

Volume parcellation for improved dynamic shimming

Michael Poole · Richard Bowtell

Received: 5 July 2007 / Revised: 11 December 2007 / Accepted: 14 December 2007
© ESMRMB 2008

Abstract

Introduction The need for a homogeneous magnetic field in magnetic resonance imaging is well established, especially at high static magnetic field strengths where susceptibility-induced image distortions and signal losses become excessively large. Dynamic shim updating, where the optimal set of shim currents is applied for each slice during a multi-slice acquisition, has been shown to improve magnetic field homogeneity to a greater extent than conventional global shimming.

Methods Here, in an initial feasibility study, we show via simulation that improved efficacy of shimming can be achieved by using the novel parcellated dynamic shimming method.

Results The results of these simulations indicate that parcellated dynamic shimming based on just linear shim terms can perform approximately as well as slice-based dynamic shimming with up to third-order shim terms.

Conclusions This work shows that the effective magnetic field inhomogeneity can be further reduced if shimming and image data acquisition are sequentially performed over a series of compact, cuboidal sub-volumes rather than planes. Further work is needed to develop an imaging approach that can be used for the optimal implementation of parcellated dynamic shimming.

Keywords Shimming · Dynamic shimming · High field · Susceptibility

Introduction

Magnetic resonance imaging (MRI) requires an intense magnetic field that has a static, uniform magnitude and orientation over the whole region of interest (ROI). However, in real MRI experiments a perfectly uniform magnetic field is never available, and there will always be some degree of magnetic field inhomogeneity, ΔB_0 . Field inhomogeneity may originate from a variety of sources each producing effects of different magnitude. A well-installed MRI scanner generates a highly homogeneous static magnetic field, B_0 , with tolerances in the magnet manufacture producing field inhomogeneities that are typically less than 0.5 parts-per-million (ppm) in magnitude over the field of view (FOV) used in imaging. However, once an object is introduced into the field, B_0 becomes more inhomogeneous. This inhomogeneity results from differences in magnetic susceptibility within the sample and in biological samples tends to have a magnitude of a few ppm. The most severe effects in the human head are seen in the inferior frontal cortex, superior to the sphenoid and ethmoid sinuses and in the inferior temporal cortex, superior to the external auditory canal and mastoid air cells [1].

Magnetic field inhomogeneity causes signal loss in gradient echo images resulting from intra-voxel phase dispersion. In general the larger voxel dimension in the slice direction means that it is field variation across the slice that most readily causes this signal attenuation, leading to regions of signal “drop-out”. Field inhomogeneity also causes image distortion resulting from the mis-registration of signals due to unwanted spatial variation of resonance frequency. This geometric distortion can be corrected using a previously acquired B_0 map and post-processing the image data [2], but the loss of signal from through-slice field variations is not recovered by this process. Echo planar imaging (EPI), which is used

M. Poole · R. Bowtell (✉)
Sir Peter Mansfield Magnetic Resonance Centre,
School of Physics and Astronomy,
University Park, Nottingham NG7 2RD, UK
e-mail: Richard.Bowtell@nottingham.ac.uk

M. Poole
e-mail: ppxmp@nottingham.ac.uk

for the majority of fMRI studies, is particularly sensitive to such distortion as a result of the relatively long signal read-out time that has to be employed. Field inhomogeneity taking the form of a gradient in the phase encoding direction also causes a shift of the apparent echo time leading to spatial variation in the sensitivity to BOLD contrast [3]. All of these effects are exacerbated at high static field strengths [4] since susceptibility-induced field inhomogeneity scales linearly with B_0 .

The field perturbation, ΔB_0 , may be approximated as a weighted linear combination of spherical harmonic basis functions [5]. MRI scanners are equipped with a set of shim coils that generate magnetic fields approximating the form of the low-order spherical harmonics. ΔB_0 is ameliorated in the shimming process by passing currents, set manually or automatically, through the shim coils. With expert knowledge of how each of the spherical harmonic ΔB_0 component manifests itself in the free induction decay (FID), currents in the shim coils can be manually adjusted to minimise the rate of signal decay [6,7]. Automatic FID shimming [8,9] involves finding the shim currents that maximise the time integral of the magnitude of the complex FID signal using search algorithms, such as the simplex algorithm (e.g., [10, Sect. 10.4]).

Prammer et al. [11] introduced the concept of measuring the spatial variation of ΔB_0 , analysing its spherical harmonic content and setting the currents in the shim coils to maximally annul ΔB_0 . Here, we refer to this technique as global shimming to distinguish it from the other methods of shimming. FASTMAP and its derivatives are time-efficient methods of acquiring the required information about ΔB_0 [12–14], and are now commonly used in clinical MRI scanners.

z -Shimming is a technique that reduces the amount of signal lost due to through-slice field variations via application of compensation gradients [15,16]. In this approach additional image data are acquired with different slice-select gradient rephase pulse amplitudes and recombined to form an image showing reduced signal loss. The need to acquire additional image data means that z -shimming extends the imaging time and is, therefore, often impractical for fMRI. Tailored radio-frequency (TRF) pulses producing non-uniform through-slice phase responses have been used to recover signal losses from severely affected regions [17–19]. However these techniques either decrease the overall SNR of the data or increase the data image acquisition time. In previous work it has been shown that shimming a small region allows the recovery of signal from that region whilst making the field in the rest of the FOV significantly worse [20,21]. In multiple acquisitions the data can be segmented and recombined to give a good signal in all areas, but again these methods require additional time to acquire.

Dynamic shimming (or dynamic shim updating, DSU) [22–24], is similar to the field-map-based shimming approach of Prammer et al. [11] in that it involves calculation of the

shim currents that maximally annul ΔB_0 . With dynamic shimming, however, this process is performed separately for each slice of a multi-slice data acquisition [22] and the shim coil currents are then changed for the acquisition of each slice. Reducing the size of the shimming volume to that of single slice sub-volumes reduces the spatial extent over which the field may vary and therefore the number of spherical harmonics needed to characterise the field variation, allowing a better average cancellation of the field inhomogeneity over the whole multi-slice volume. Implementation of dynamic shimming, however generally requires the scanner hardware to be modified, since in most systems the shim coils and power supplies are not designed to allow the shim currents to be changed on the time-scale of an individual slice acquisition.

In this work we expand upon the dynamic shimming idea and propose parcellated dynamic shimming, in which the sub-volumes used in acquisition are cuboids rather than slices [25]. This approach further reduces the spatial extent of the sub-volume over which shimming is performed so that ΔB_0 is better approximated by a limited number of spherical harmonic terms. We test the efficacy of this approach by simulation of the effects of global, slice-based dynamic and parcellated dynamic shimming on magnetic field maps spanning the whole brain, which were acquired from 11 subjects.

Methods

Magnetic field inhomogeneity data

Field maps spanning the whole brain were acquired using a dual-echo, 3D gradient echo sequence, with echo times $T_{E1} = 2.2$ ms and $T_{E2} = 20.0$ ms on a Philips 3T Achieva MRI scanner. Each data set took less than 2 min to acquire. The phase of the images generated from the two different echoes was unwrapped [26], followed by subtraction and scaling of the resulting difference images to yield maps of the magnetic field offset, expressed in ppm of the static magnetic field. The phase maps are automatically masked by thresholding the skull-stripped [27] magnitude images prior to phase unwrapping. Eleven such ΔB_0 data sets were acquired from consenting, healthy volunteers with 2 mm isotropic resolution and a matrix size of $96 \times 96 \times 66$, which was zero padded to $96 \times 96 \times 96$. This zero padding allowed the total volume to be simply divided up into similar numbers of parcels as the image sub-volume dimensions were varied at fixed sub-volume size (e.g., allowing comparison of the performance of a $48 \times 12 \times 8$ sub-volume scheme to a $12 \times 8 \times 48$ scheme). Subjects were positioned in the magnet with the nasion at isocentre and with the orientation of the head constrained only by the relatively tight fitting eight-channel RF coil (inside diameter = 230 mm). Precise

control of the position and orientation of the subject's head within the FOV was not desired since we aimed to use data that were representative of typical fMRI studies. A magnetic field map for each shim coil (up to and including third-order shims) was generated by calculation of the appropriate spherical harmonic on the matrix of points at which the field data, $\Delta B_0(\mathbf{r})$, were measured with the centre of the FOV defining the isocentre of the generated field maps. Such maps may also, and more accurately, be obtained by directly mapping the field generated by actual shim coils.

Global shimming

The shim currents, I^{shim} , required for shimming can be obtained by pseudo-inversion (indicated by the \dagger symbol), of a matrix describing the shim fields, $\mathbf{B}_0^{\text{shim}}$, multiplied by the field required to maximally null ΔB_0

$$I^{\text{shim}} = -\Delta B_0 \left(\mathbf{B}_0^{\text{shim}} \right)^\dagger \quad (1)$$

where $I^{\text{shim}} = [I^{\{0,0\}}, I^{\{1,0\}}, I^{\{1,1\}}, \dots, I^{\{n,m\}}]$ and $\mathbf{B}_0^{\text{shim}} = [\mathbf{B}_0^{\{0,0\}}, \mathbf{B}_0^{\{1,0\}}, \mathbf{B}_0^{\{1,1\}}, \dots, \mathbf{B}_0^{\{n,m\}}]$. $I^{\{n,m\}}$ is the current to be passed through the shim coil that produces the spherical harmonic with order n and degree m , and $\mathbf{B}_0^{\{n,m\}}$ is the magnetic field generated at the set of measurement points by passing 1 A current through the $\{n, m\}$ shim coil.

Slice-based dynamic shimming

In slice-based dynamic shimming [22], Eq. (1) is solved separately for each imaging slice. The calculated currents are then applied to the shim coils for the time period in which the appropriate slice is being imaged. In this case ΔB_0 and $\mathbf{B}_0^{\text{shim}}$ only contain magnetic field values from the single slice that is currently being imaged, meaning that ΔB_0 becomes essentially 2D in slice-based dynamic shimming. This means that the fields from some shim coils become degenerate. For example, in dynamic shimming where axial slices are acquired and shimmed individually, z is constant throughout the sub-volume and therefore the Z0 shim and Z-gradient terms become degenerate. Similarly, the X-gradient and ZX shim terms (and also the Y-gradient and ZY shim terms) become degenerate. Through-slice gradients can still detrimentally affect the quality of the image. A magnetic field variation through the slice will cause dephasing and signal loss. The issue of shim degeneracy and through-slice linear gradients for oblique slices has been discussed more fully by Koch et al. [28].

Parcellated dynamic shimming

Equation (1) is solved for each sub-volume in parcellated dynamic shimming, but now ΔB_0 and $\mathbf{B}_0^{\text{shim}}$ contain values

from a small cuboidal region. Slice-based dynamic shimming can be viewed as a special case of parcellated shimming in which the shimming sub-volume has two dimensions that are the same in extent as those of the whole imaging volume, while being only one voxel thick in the third dimension.

In this work we investigate how the geometry of the sub-volumes affects the efficacy of shimming. To characterise the geometry of the sub-volumes used in the parcellation, we introduce a dimensionless ‘‘compactness’’ parameter, C , where

$$C = \frac{\sqrt[3]{V}}{\sqrt{VA}}. \quad (2)$$

Here V describes the size of the shimming sub-volume while SA is its surface area, so that C is large for compact sub-volume geometries (e.g., cubes) and small for flat geometries with large extent (e.g., thin slabs). The efficacy of shimming, ε , was characterised using the percentage change due to shimming of the standard deviation of ΔB_0 measured over the whole imaging volume:

$$\varepsilon = \frac{\sigma_{\text{pre}} - \sigma_{\text{post}}}{\sigma_{\text{pre}}} \times 100 \quad (3)$$

where $\sigma_{\text{pre}} = \|\Delta B_0\|$ and $\sigma_{\text{post}} = \|\Delta B_0 - I^{\text{shim}} \mathbf{B}_0^{\text{shim}}\|$ and $\|\cdot\|$ denotes the l^2 -norm.

Parcellation schemes

The way in which the imaging volume is subdivided is referred to as the ‘‘parcellation scheme’’ and is defined by the dimensions of the sub-volume, written as $N_x \times N_y \times N_z$. N_x , N_y and N_z describe the numbers of voxels spanning the left–right, anterior–posterior and foot–head dimensions of the sub-volume. For instance, for the data analysed here, dynamic shimming based on axial slices would be termed the $96 \times 96 \times 1$ scheme, while a more compact parcellation scheme might employ a $24 \times 24 \times 16$ sub-volume size. These two sub-volumes have the same volume, $V = 9,216$ voxels (or $73,728 \text{ mm}^3$), but compactness values of 0.153 and 0.404, respectively. In this work we chose that any dimension could be subdivided into 1, 2, 3, 4, 6, 8, 12, 18, 24, 32, 48, or 96 parts. If the scan size is not conveniently factorised, the image data may simply be cropped or zero-padded to a convenient size. We also prescribed that the minimum volume for a parcellation scheme would be 9,216 voxels. There are 313 different possible parcellation schemes that conform to these criteria with volumes ranging from 9,216 to 884,736 voxels and compactness values from $C = 0.153$ to 0.408. Figure 1 shows the shapes of all the sub-volumes for parcellation schemes using 9,216 voxels. The effect of first, second and third-order shimming was simulated for each parcellation scheme using data from all 11 subjects and the resulting values of shimming efficacy, ε , recorded.

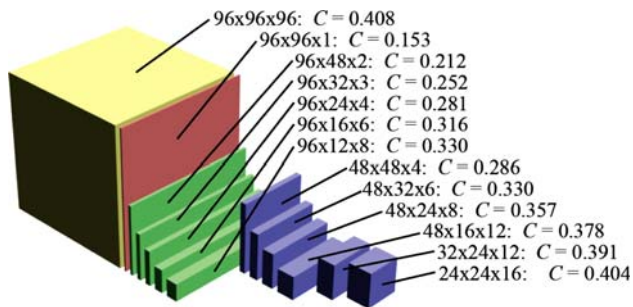


Fig. 1 Sub-volumes that contain 9,216 voxels used in parcellation of a $96 \times 96 \times 96$ voxel-sized region. Permutation of the sub-volume dimensions along the three Cartesian axes can be used to produce other parcellation schemes (e.g., $96 \times 96 \times 1$, $96 \times 1 \times 96$, $1 \times 96 \times 96$). The full imaging volume is also shown

A convenient way to categorise the 313 different parcellation schemes is to consider the number of dimensions of the full imaging volume that the sub-volume fully spans. Clearly, the global shimming ($96 \times 96 \times 96$) volume spans the imaging volume in all three dimensions, x , y , and z (sub-volume shown in yellow in Fig. 1), and in the slice-based dynamic shimming schemes the sub-volume spans two dimensions of the full volume (red in Fig. 1). In 195 of the 313 schemes the sub-volume spans just one full dimension (green in Fig. 1), while in the remaining 114 cases the sub-volumes have no dimensions that span the whole imaging volume (blue in Fig. 1). Parcellation schemes in which the sub-volume spans at least one dimension of the whole volume are likely to be more straightforward to implement practically.

Current constraints

In the simulations discussed so far in this work, the restrictions on the shim coil currents that are inevitably present in a real system have not been considered. We now go on to describe the effects of limiting the shim currents. The amount of current that can be passed through a shim coil is limited by resistive heating effects and the capacity of the power supply used to drive the coil. This in turn limits the magnitude of the spherical harmonic that a particular shim coil is capable of generating. Simply truncating the current to the maximum allowed value when the calculation prescribes a greater than possible current leads to a non-optimal shim; it is better to take into account the current limitations when solving Eq. (1) [29]. Here we simulate the effect on ε of placing a restriction on the amount of available current, I^{\max} , for some of the different parcellation schemes when considering up to and including second order shims. This was accomplished by using the `lsqlin` function in Matlab's Optimisation Toolbox[®], which uses a subspace trust region method based on the interior-reflective Newton method as described in [30]. In these calculations, the shim coil efficiencies

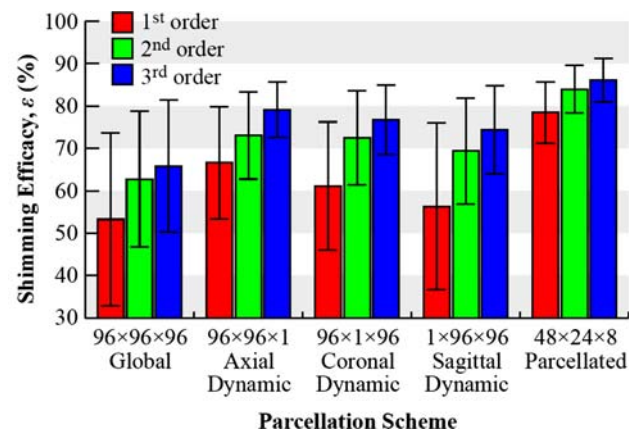


Fig. 2 Efficacy of shimming, ε , for global, slice-based dynamic, and best parcellated shimming schemes averaged over all 11 subjects. Results for shimming using up to first, second, and third order shim terms are shown. In each case the *error bars* indicate the standard deviation of ε over all subjects

were based on values previously obtained from designing coils for an insertable gradient and second-order shim coil set [31]. These coils were designed using a distributed wire pattern, arbitrary geometry technique [31–33] to have high efficiency and low inductance, in order to allow the currents in the shims to be switched rapidly during implementation of dynamic shimming. The coil efficiencies, η are given in $\text{m T m}^{-n} \text{A}^{-1}$ in Table 1, where n is the order of the coil.

Results

The results produced by simulating the effect of the various shimming schemes on the measured field maps are shown in Figs. 2, 3, 4, 5, and 6. Figure 2 shows a comparison of the efficacy of global shimming, axial, coronal and sagittal slice-based dynamic shimming and the best performing parcellation scheme averaged over all 11 subjects. In each case, the figure shows the results for shimming with all shim terms up to first-order, second-order, and third order, and the error bars on the graph indicate the standard deviation of measurements over all subjects.

Figure 3 shows the variation of the efficacy of shimming as a function of the compactness for all parcellation schemes that employ 9,216 voxels per sub-volume, while Fig. 4 shows how the efficacy of shimming varies with the cube-rooted volume of the sub-volume parcellation scheme. The way in which constraining the current in the shims, based on the shim coil efficiencies detailed in Table 1, affects the efficacy of shimming at 3 T for second-order shimming with the $96 \times 96 \times 96$, $96 \times 96 \times 1$, $96 \times 12 \times 8$ and $48 \times 24 \times 8$ parcellation schemes is demonstrated in Fig. 5. These curves will move towards lower currents with an increase in magnetic

Table 1 Shim field equations and efficiencies for shim coils up to second-order

Shim type	{Order, degree} { n, m }	Field equation	Efficiency, η ($\mu\text{T m}^{-n} \text{A}^{-1}$)
Z0	{0, 0}	1	9.1
Z	{1, 0}	z	121
X	{1, 1}	x	100
Y	{1, -1}	y	119
Z2	{2, 0}	$z^2 - \frac{1}{2}(x^2 + y^2)$	340
ZX	{2, 1}	$3zx$	360
ZY	{2, -1}	$3zy$	411
X2–Y2	{2, 2}	$3(x^2 - y^2)$	181
XY	{2, -2}	$6xy$	252

Here n and m are the order and degree of the spherical harmonic

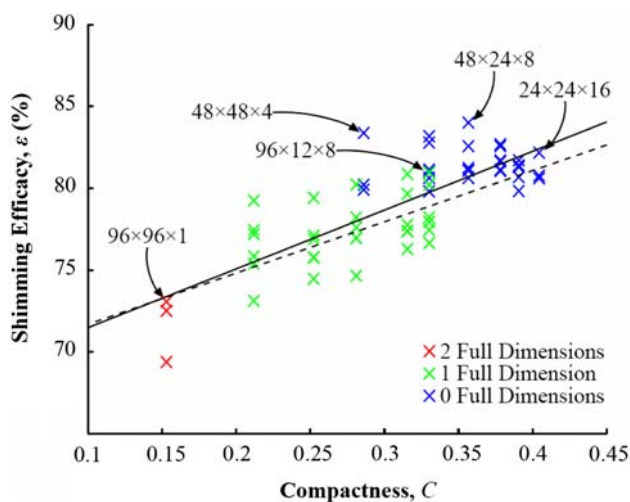


Fig. 3 ε Versus C for second-order parcellated dynamic shimming for schemes containing 9,216 voxels per sub-volume. Schemes employing sub-volumes with 2, 1 and 0 dimensions that span the whole imaging volume are shown in red, green and blue, respectively, and some potentially useful schemes are labelled. Linear regression lines are plotted for all the data (solid line) and just for those schemes with sub-volumes spanning 1 or 2 full image volume dimensions (dashed line)

field strength. These are the best performing schemes using sub-volumes that span 3, 2, 1 and 0 dimensions of the full imaging volume. A range of logarithmically spaced current limits were used from 0.001 to 10 A.

Axial, coronal and sagittal anatomical images and field maps along with histograms of ΔB_0 based on data from one representative subject are shown in Fig. 6 for different shimming schemes. This demonstrates the homogeneity improvement that can be gained by using slice-based dynamic rather than global shimming, and the further improvement that can be achieved using parcellated dynamic shimming.

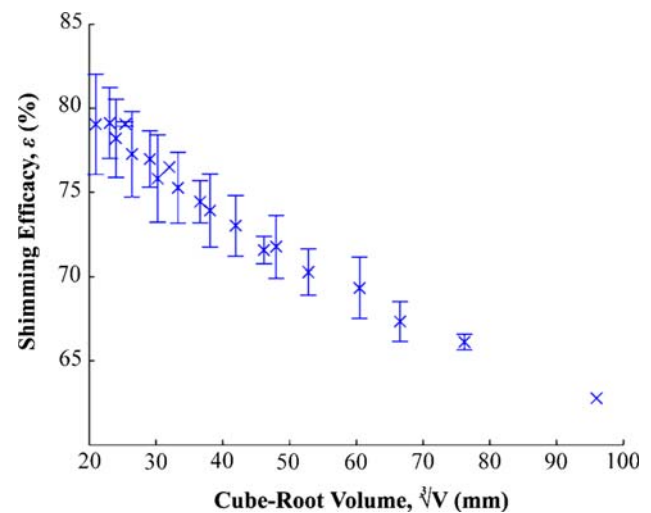


Fig. 4 The mean shimming efficacy for each different parcellation volume against the cube-root of the volume. Error bars indicate one standard deviation above and below the mean

Discussion

The simulated results shown in Fig. 2 demonstrate that when zeroth- to third-order shims are used, ε is increased by up to 14% by using slice-based dynamic shimming rather than global shimming and by up to 22% by using the best-performing parcellation scheme in which the sub-volume is $48 \times 24 \times 8$ pixels in size. Similar fractional gains in efficacy occur when shims of up to only second or first order are used. The best shimming efficacy is achieved with conventional slice-based shimming when axial slices are used. Figure 2 also shows that, as would be expected, ε increases for all shimming schemes as the number of shim terms is increased to include second and then third-order terms. Interestingly, however, the best parcellated scheme employing first-order shims only yields a similar shimming efficacy to that achieved using the slice-based dynamic shimming scheme with

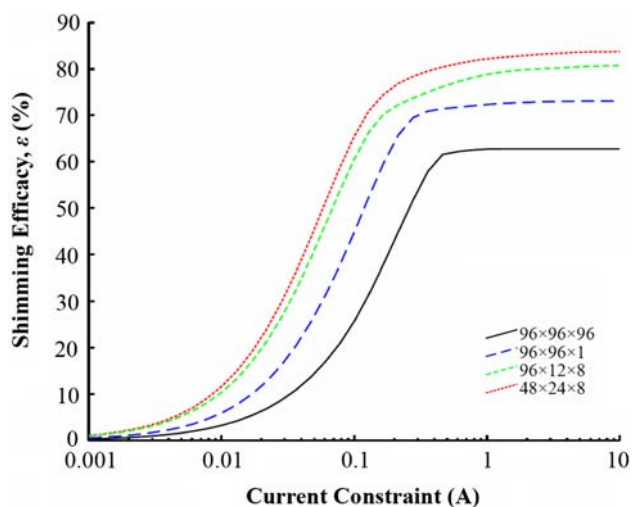


Fig. 5 The variation of the shimming efficacy as the maximum absolute current limit is altered for the $96 \times 96 \times 96$, $96 \times 96 \times 1$, $96 \times 12 \times 8$ and $48 \times 24 \times 8$ parcellation schemes, assuming operation at 3 T

up to third-order shim terms included. It can also be seen from Fig. 2 that the standard deviation of ε is significantly smaller for the best parcellated scheme, indicating that this approach is better able to cope with the natural variation of ΔB_0 across the 11 subjects. Figure 6 demonstrates that the strong, local field inhomogeneity occurring in the inferior frontal cortex and above the ear canals is better eliminated by using the best parcellated scheme rather than the conventional or slice-based dynamic shimming approaches.

Figure 4 shows that on average the efficacy of shimming increases as the size of the sub-volume used for parcellated dynamic shimming is decreased. Figure 3 demonstrates that at fixed volume the efficacy of shimming increases in an approximately linear fashion with the compactness of the sub-volume. These findings result from the fact that it is possible to generate a better representation of the typical spatial pattern of ΔB_0 found in the head with a relatively small number of low order spherical harmonics, when the fitting is applied separately within small sub-volumes which have similar spatial extent in all three dimensions.

Although there is a linear trend for ε to increase with C , the parcellation scheme that performed best on average over the 11 subjects studied here was that with sub-volume dimensions of $48 \times 24 \times 8$ ($C = 0.357$). The fact that the best scheme is not the most compact indicates that the choice of resolution, FOV and the specific morphology of ΔB_0 for each subject are important factors in determining the performance of different parcellation schemes. The excellent performance of the $48 \times 24 \times 8$ scheme suggests that segmentation of the volume into many partitions in the inferior–superior direction is most advantageous. This is consistent with the finding that slice-based, dynamic shimming using

axial slices outperforms the schemes employing coronal or sagittal slice orientation, and probably results from the limited axial extent of the strong local field distortions that are generated in the inferior frontal cortex, superior to the sphenoid and ethmoid sinuses, and the inferior temporal cortex superior to the external auditory canal and mastoid air cells. ΔB_0 generally exhibits reflectional symmetry about the central sagittal slice, which is one possible reason that schemes which only divide the x -direction into two halves perform well. Also, parcellation schemes that have one dimension spanning the imaging volume in the x -direction generally outperform those spanning the y or z -directions.

Figure 5 shows the way in which limiting the current in the shims alters ε . It is evident that ε begins to decrease earlier as the current limit is lowered for slice-based, dynamic shimming and more so for parcellated dynamic shimming, indicating that more intense shim fields are required for these schemes if they are to achieve their full potential. If the currents in the shim coils were simply truncated to their maximum values after fitting, the advantage of using parcellated dynamic shimming may be lost, and it is therefore important to take the current limits into account when calculating the shim currents. Actual current limits will depend on the properties of the gradient and shim coils and of the power supplies with which they are driven and so will vary from system to system.

By reducing the net magnetic field inhomogeneity, parcellated dynamic shimming should allow images with less distortion and signal drop-out to be obtained. However, the implementation of an imaging protocol that is compatible with parcellated dynamic shimming has yet to be demonstrated. Ideally, the shimming, signal excitation, and acquisition protocols should be compatible and introduce no extra time penalty, reduction of signal-to-noise (SNR) or loss of sensitivity to functional activity over established methods for high speed brain imaging. Echo volumar imaging (EVI) [34] provides the most promising platform for implementation of parcellated dynamic shimming since it allows the acquisition of data from a cuboidal region in a single shot and previous work has shown that EVI can be combined with outer volume suppression (OVS) [35] so as to generate image data from a sub-volume of the human brain [36].

The use of OVS is however problematic when trying to sequentially scan multiple sub-volumes so as to acquire data rapidly from a whole imaging volume. This is because the OVS module used when acquiring data from one sub-volume leads to suppression of the magnetisation from other sub-volumes, necessitating the acceptance of a loss of signal intensity or an increase in TR to allow more time for longitudinal magnetisation to recover. A more promising approach may be to use 2D or 3D spatially selective tailored radio-frequency pulses (SSTRF) [37–40] to excite the signal from the sub-volumes. Although such pulses tend to be long in

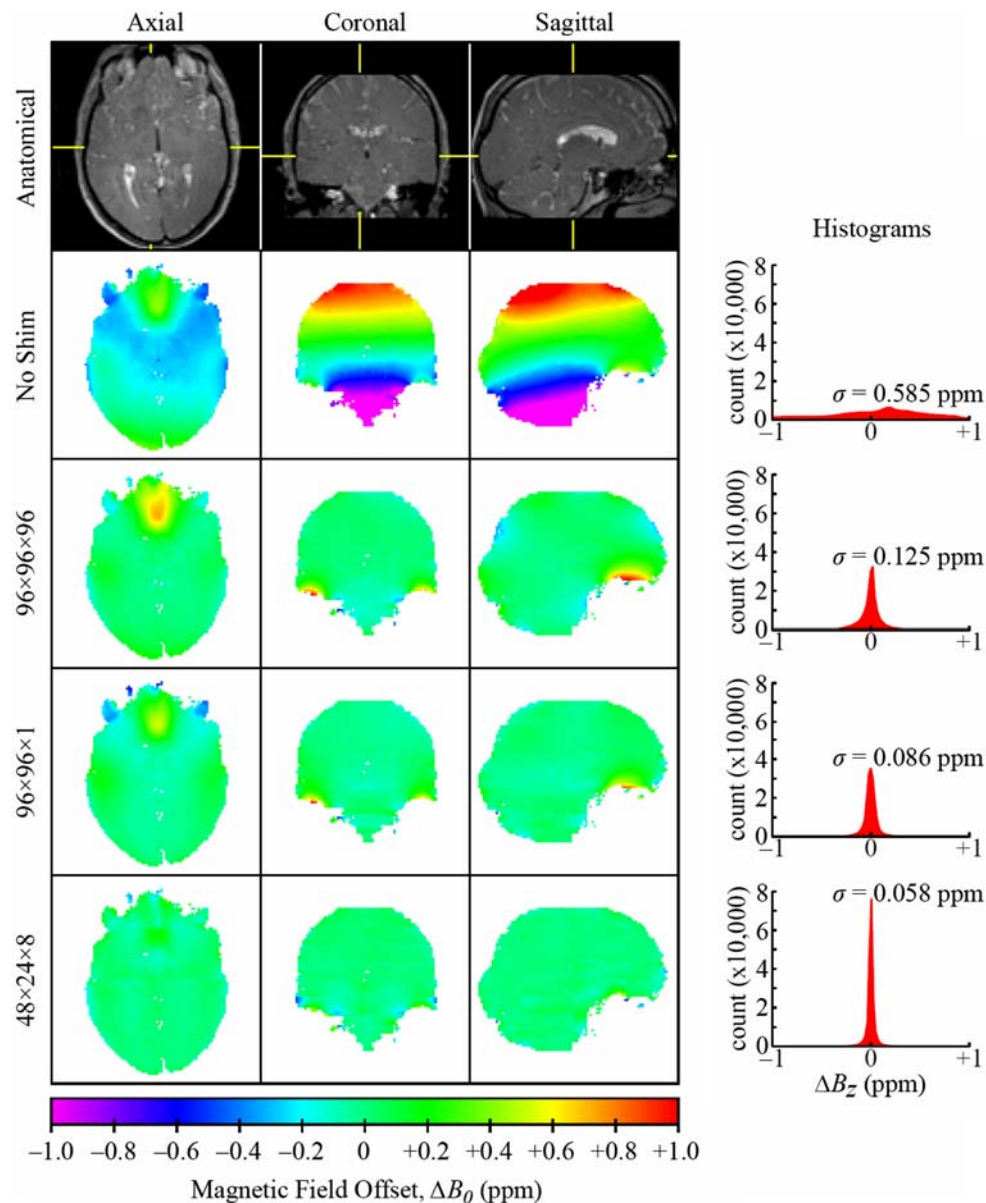


Fig. 6 Anatomical images showing the slice positions and maps of the magnetic field offset in *sagittal*, *coronal*, and *axial* slices of one subject before and after second-order shimming using the $96 \times 96 \times 96$,

$96 \times 96 \times 1$ and $48 \times 24 \times 8$ parcellation schemes. *Histograms* and RMS values, σ , of the magnetic field offset for each scheme are also shown

duration and sensitive to off-resonance effects, parallel transmission techniques, such as transmit SENSE [41] have been shown to be capable of ameliorating these problems, potentially making the use of 3D-SSTRF pulses in conjunction with EVI a viable method for carrying out parcellated dynamic shimming. The greater ease of implementation of 2D rather than 3D-SSTRF pulses means that parcellation schemes that only require that selective excitation defines the volume in two spatial dimensions are more likely to be experimentally feasible. Parcellation schemes in which at least one dimension of the sub-volume spans the whole imaging

volume fulfil this requirement and so their performance has been separately highlighted in the “Results” and “Discussion” sections. It is also important to note that both OVS and SSTRF techniques are affected by magnetic field inhomogeneity, and this issue will have to be addressed in a practical implementation of parcellated shimming.

Band-pass filtering of the NMR signal can also be used to limit the extent of the imaged sub-volume in the read direction, thus reducing the required dimensionality of the selective excitation by one, but with this approach the magnetisation in more than one sub-volume would be excited during

each acquisition leading to a similar loss of sensitivity during sequential acquisition of sub-volumes to that which would occur when OVS is employed. Figure 4 shows that reducing the size of the sub-volume increases the efficacy of parcelled dynamic shimming, but such a reduction clearly also increases the number of sub-volumes from which data must be acquired in order to sample the whole imaging volume. If this number becomes too large, the minimum accessible TR will have to be increased to accommodate all of the sub-volume acquisitions. Further exploration of the compromise between shimming efficacy and minimum accessible TR via variation of the sub-volume size is needed.

With a fixed signal acquisition window length (and consequently fixed sensitivity to field inhomogeneity induced distortion) and fixed image resolution, the number of echoes that can be acquired in an EVI sequence is limited by the accessible strength and slew rate of the read gradient. Applying the read gradient along the direction corresponding to the dimension of the sub-volume of greatest spatial extent is therefore likely to be advantageous, since this requires the minimum number of echoes in the EVI acquisition. It is worth noting that parallel imaging techniques [42] can be used to reduce further the number of echoes that need to be acquired. In the case of the $48 \times 24 \times 8$ parcellation scheme which was shown to provide the best shimming efficacy, the optimal approach would be to apply the read gradient in the x -direction, so that the EVI sequence would require the acquisition of $24 \times 8 = 192$ echoes. Application of SENSE with an acceleration factor of two (applied in the y -direction) would reduce this number to a more reasonable value of 96. Further reduction in this number could be achieved via use of a 2D acceleration.

Shim terms that show similar in-plane field variation, but which have different dependence on the slice-direction co-ordinate become degenerate in slice-based dynamic shimming schemes. This reduces the number of shim terms available for shimming. However through-slice linear gradients may still cause signal loss in images. This can be ameliorated by taking into account the field measured in the slices that are adjacent to the imaging slice and applying a gradient that is the inverse of the average through-slice gradient.

If the parcelled dynamic shimming method is considered to be a generalisation of global and dynamic shimming, a further generalisation could be conceived involving a subdivision of the imaging volume into cuboidal sub-volumes of varying size. With this approach, it may offer some benefit to use large sub-volumes in areas of the brain where small variations in ΔB_0 occur and to use smaller sub-volumes in other regions where ΔB_0 has higher intensity and varies more rapidly with position. The excellent shimming that can be observed from the parcelled scheme field map images in Fig. 6 is achieved in part because the boundary between adjacent sub-volumes falls within the area of high field

inhomogeneity in the inferior frontal cortex. An adaptive mesh refinement (AMR) algorithm [43] based on the shape of the measured ΔB_0 may be able to decide the best arbitrary subdivision of the whole volume. Furthermore, employing non-cuboidal, tessellating sub-volumes provides an even more generalised approach, which would yield more efficient shimming, although combining these more generalised concepts with imaging protocols would be very difficult indeed.

The shimming efficacy measure, ε , is a good parameter for estimating the reduction in ΔB_0 . It is not possible, however, to achieve $\varepsilon = 100\%$ since some noise and errors are inevitably present in the field maps. Noise in the field maps may simply arise from random noise in the measured phase maps. More significant errors in the field map occur from chemical shift differences of tissues in the body, flow, incorrect masking of the brain region and from the phase-unwrapping algorithm. The phase-unwrapping algorithm used in this work [26] first unwraps each slice of the data sequentially and then unwraps in the third dimension. Any unconnected brain regions within a slice may not have consistent unwrapped phase and therefore erroneous ΔB_0 values are recorded. A 3D phase unwrapping algorithm would eliminate these errors (e.g., [44]).

Conclusions

The primary aim of this paper is to show that parcelled dynamic shimming potentially provides a more effective method than conventional slice-based dynamic shimming in reducing the magnetic field inhomogeneities in the head. This has been achieved by simulated shimming of 3D magnetic field inhomogeneity maps obtained from 11 subjects with a dual-echo, 3D gradient echo field mapping sequence. The efficacy of shimming was calculated from the standard deviation of the field inhomogeneity calculated before and after shimming. Using up to second-order shim terms, global (whole volume), slice-based dynamic, and parcelled dynamic shimming were found to yield shimming efficacies of $63 \pm 16\%$, $73 \pm 10\%$ and $84 \pm 6\%$, respectively. The results obtained in this work indicate that greater improvements in magnetic field homogeneity, can be gained via implementation of parcelled dynamic shimming with only first-order shims than is possible with global or slice-based dynamic shimming using up to third-order shim terms.

These findings indicate that it is certainly worthwhile to pursue an experimental implementation of parcelled dynamic shimming and it is hoped that this publication will stimulate further work in this area. We have identified the use of EVI in conjunction with volume selective excitation as the best way of experimentally realising the advantages of the parcelled shimming approach and are working towards its

implementation at 7 T. The development of robust parallel imaging approaches for use with EVI and implementation of short-duration, 2D or 3D-SSTRF pulses at 7 T form the current focus of this effort.

While the work described here has focused on homogenising the magnetic field generated by susceptibility differences of tissues inside the human head, parcellated dynamic shimming is a general technique that could be applied to other parts of the body, or to other species. The motivation for this focus was the desire to provide an approach allowing sensitivity losses and image distortion in functional studies of brain activity, to be minimised, particularly at high static field strengths (≥ 3 T) where these effects become increasingly severe.

References

- Li S, Dardzinski BJ, Collins CM, Yang QX, Smith MB (1996) Three-dimensional mapping of the static magnetic field inside the human head. *Magn Reson Med* 36(5):705–714
- Sumanaweera TS, Glover GH, Binford TO, Adler JR (1993) MR susceptibility misregistration correction. *IEEE Trans Med Imaging* 12:251–259
- Deichmann R, Josephs O, Hutton C, Corfield DR, Turner R (2002) Compensation of susceptibility-induced BOLD sensitivity losses in echo-planar fMRI imaging. *Neuroimage* 15(1):120–135
- Farahani K, Sinha U, Sinha S, Chiu LC-L, Lufkin RB (1990) Effect of field strength on susceptibility artifacts in magnetic resonance imaging. *Comput Med Imaging Graph* 14(6):409–413
- Roméo F, Hoult DI (1984) Magnet field profiling: analysis and correcting coil design. *Magn Reson Med* 1(1):44–65
- Conover W (1984) Practical guide to shimming superconducting NMR magnets, Chap 2. Wiley, New York, pp 37–51
- Chmurny GN, Hoult DI (1990) The ancient and honourable art of shimming. *Concepts Magn Reson* 2(3):131–149
- Tochtrop M, Vollmann W, Holz D, Leussler C (1987) Automatic shimming of selected volumes in patients. *Proc Soc Magn Reson Med* 6:816
- Holz D, Jensen D, Proksa R, Tochtrop M, Vollmann W (1988) Automatic shimming for localized spectroscopy. *Med Phys* 15(6):898–903
- Press WH, Flannery BP, Teukolsky SA, Vetterling WT (1992) Numerical recipes in C: the art of scientific computing. Cambridge University Press, Cambridge
- Prammer MG, Haselgrove JC, Shinnar M, Leigh JS (1988) A new approach to automatic shimming. *J Magn Reson* 77:40–52
- Gruetter R, Boesch C (1992) Fast, noniterative shimming of spatially localized signals. In vivo analysis of the magnetic field along axes. *J Magn Reson* 96:323–334
- Gruetter R (1993) Automatic, localized in vivo adjustment of all first- and second-order shim coils. *Magn Reson Med* 29(6):804–811
- Klassen LM, Menon RS (2004) Robust automated shimming technique using arbitrary mapping acquisition parameters (RASTAMAP). *Magn Reson Med* 51(5):881–887
- Frahm J, Merboldt KD, Hänicke W (1988) Direct FLASH MR imaging of magnetic field inhomogeneities by gradient compensation. *Magn Reson Med* 6(4):474–480
- Yang QW, Dardzinski BJ, Li S, Eslinger PJ, Smith MB (1997) Multi-gradient echo with susceptibility inhomogeneity compensation (MGESIC): demonstration of fMRI in the olfactory cortex at 3.0T. *Magn Reson Med* 37(3):331–335
- Cho ZH, Ro YM (1992) Reduction of susceptibility artefact in gradient-echo imaging. *Magn Reson Med* 23(1):193–200
- Chen N-K, Wyrwicz AM (1999) Removal of intravoxel dephasing artifact in gradient echo images using a field-map based RF refocussing technique. *Magn Reson Med* 42(2):807–812
- Stenger VA, Boada FE, Noll DC (2000) Three dimensional tailored rf pulses for the reduction of susceptibility artifacts in T2*-weighted functional MRI. *Magn Reson Med* 44(4):525–531
- Schneider E, Glover G (1991) Rapid in vivo proton shimming. *Magn Reson Med* 18:335–347
- Wilson JL, Jenkinson M, de Araujo I, Kringelbach ML, Rolls ET, Jezzard P (2002) Fast, fully automated global and local magnetic field optimization for fMRI of the human brain. *Neuroimage* 17:967–976
- Blamire AM, Rothman DL, Nixon T (1996) Dynamic shim updating: a new approach towards optimized whole brain shimming. *Magn Reson Med* 36(1):159–165
- Morrell G, Spielman D (1997) Dynamic shimming for multi-slice magnetic resonance imaging. *Magn Reson Med* 38(3):477–483
- de Graaf RA, Brown PB, McIntyre S, Rothman DL, Nixon TW (2003) Dynamic shim updating (DSU) for multislice signal acquisition. *Magn Reson Med* 49(3):409–416
- Poole M, Bowtell R (2007) Evaluation of parcellated dynamic shimming. ISMRM workshop on advances in high field MR, 5
- Saad N, Peled S (2005) Easy 3D phase unwrapping. *Proc Int Soc Magn Reson Med* 13:2251
- Smith SM (2002) Fast, robust automated brain extraction. *Human Brain Map* 17:143–155
- Koch KM, McIntyre S, Nixon TW, Rothman DL, de Graaf RA (2006) Dynamic shim updating on the human brain. *J Magn Reson* 180(2):286–296
- Wen H, Jaffer FA (1995) An in vivo automated shimming method taking into account shim current constraints. *Magn Reson Med* 34(6):898–904
- Coleman TF, Li YY (1996) An interior trust region approach for nonlinear minimization subject to bounds. *SIAM J Optim* 6(2):418–445
- Poole M, Bowtell R (2007) Novel gradient coils designed with a boundary element method. *Concepts Magn Reson B Magn Reson Eng* 31(3):162–175
- Pissanetzky S (1992) Minimum energy MRI gradient coils of general geometry. *Meas Sci Technol* 3(7):667–673
- Lemdiasov RA, Ludwig R (2005) A stream function method for gradient coil design. *Concepts Magn Reson B Magn Reson Eng* 26(1):67–80
- Mansfield P, Howseman AM, Ordidge RJ (1989) Volumar imaging using NMR spin echoes: echo-volumar imaging (EVI) at 0.1 t. *J Phys E* 22(5):324–330
- Singh S, Rutt BK, Henkelman RM (1990) Projection presaturation: a fast and accurate technique for multidimensional spatial localization. *J Magn Reson* 87(3):567–583
- van der Zwaag W, Francis S, Bowtell RW (2006) Improved echo volumar imaging (EVI) for functional MRI. *Magn Reson Med* 56(6):1320–1327
- Pauly JM, Hu BS, Wang SJ, Nishimura DG, Macovski A (1993) A three-dimensional spin-echo or inversion pulse. *Magn Reson Med* 29(1):2–6
- Stenger VA, Boada FE, Noll DC (2000) Three-dimensional tailored RF pulses for the reduction of susceptibility artifacts in T2*-weighted functional MRI. *Magn Reson Med* 44(4):525–531
- Stenger VA, Boada FE, Noll DC (2003) Variable-density spiral 3D tailored RF pulses. *Magn Reson Med* 50(5):1100–1106

40. Bottomley PA, Hardy CJ (1987) Two-dimensional spatially selective spin inversion and spin-echo refocusing with a single nuclear magnetic resonance pulse. *J Appl Phys* 62(10):4284–4290
41. Katscher U, Bornert P, Leussler C, van den Brink JS (2003) Transmit SENSE. *Magn Reson Med* 49(1):144–150
42. Preussmann KP, Weiger M, Scheidegger MB, Boesiger P (1999) SENSE: sensitivity encoding for fast MRI. *Magn Reson Med* 42:952–962
43. Berger MJ, Colella P (1989) Local adaptive mesh refinement for shock hydrodynamics. *J Comput Phys* 82(1):64–84
44. Xu W, Cumming I (1999) A region-growing algorithm for InSAR phase unwrapping. *IEEE Trans Geosci Remote Sens* 37:124–134